


# Benchmark performance of low-cost $\text{Sb}_2\text{Se}_3$ photocathodes for unassisted solar overall water splitting

Wooseok Yang <sup>1,4</sup>, Jin Hyun Kim<sup>2,4</sup>, Oliver S. Hutter <sup>3</sup>, Laurie J. Phillips <sup>3</sup>, Jeiwan Tan<sup>1</sup>, Jaemin Park<sup>1</sup>, Hyungsoo Lee<sup>1</sup>, Jonathan D. Major<sup>3</sup> , Jae Sung Lee<sup>2</sup>  & Jooho Moon <sup>1</sup> 

Determining cost-effective semiconductors exhibiting desirable properties for commercial photoelectrochemical water splitting remains a challenge. Herein, we report a  $\text{Sb}_2\text{Se}_3$  semiconductor that satisfies most requirements for an ideal high-performance photoelectrode, including a small band gap and favourable cost, optoelectronic properties, processability, and photocorrosion stability. Strong anisotropy, a major issue for  $\text{Sb}_2\text{Se}_3$ , is resolved by suppressing growth kinetics via close space sublimation to obtain high-quality compact thin films with favourable crystallographic orientation. The  $\text{Sb}_2\text{Se}_3$  photocathode exhibits a high photocurrent density of almost  $30 \text{ mA cm}^{-2}$  at 0 V against the reversible hydrogen electrode, the highest value so far. We demonstrate unassisted solar overall water splitting by combining the optimised  $\text{Sb}_2\text{Se}_3$  photocathode with a  $\text{BiVO}_4$  photoanode, achieving a solar-to-hydrogen efficiency of 1.5% with stability over 10 h under simulated 1 sun conditions employing a broad range of solar fluxes. Low-cost  $\text{Sb}_2\text{Se}_3$  can thus be an attractive breakthrough material for commercial solar fuel production.

<sup>1</sup>Department of Materials Science and Engineering, Yonsei University, 50 Yonsei-ro, Seodaemun-gu, Seoul 03722, Republic of Korea. <sup>2</sup>School of Energy and Chemical Engineering, Ulsan National Institute of Science and Technology, Ulsan 44919, South Korea. <sup>3</sup>Stephenson Institute for Renewable Energy, Physics Department, University of Liverpool, Liverpool L69 7XF, UK. <sup>4</sup>These authors contributed equally: Wooseok Yang, Jin Hyun Kim. email: [Jon.Major@liverpool.ac.uk](mailto:Jon.Major@liverpool.ac.uk); [jlee1234@unist.ac.kr](mailto:jlee1234@unist.ac.kr); [jmoon@yonsei.ac.kr](mailto:jmoon@yonsei.ac.kr)

**M**olecular hydrogen production via photoelectrochemical (PEC) splitting of water is a promising solution toward a zero-carbon-based society. In order to produce sustainable  $H_2$  for a scale commensurate with the global energy demand, high efficiency and low cost, both of which highly depend on the semiconductor materials used in the PEC system, should be achieved. As the solar-to-hydrogen (STH) efficiency of PEC devices using expensive photovoltaic-grade III–V semiconductors has approached the theoretical maximum<sup>1</sup>, the research community is now recognising the importance of exploring low-cost materials exhibiting good optoelectronic properties<sup>2</sup>. With this consideration, nearly all recent critical evaluations<sup>3–5</sup> pertaining to artificial photosynthesis have urged the development of new light absorbers. According to theoretical calculations<sup>6,7</sup>, two different light absorbers—having a band gap ( $E_g$ ) of  $\sim 1.8$  eV for the top electrodes and 1.0–1.3 eV for the bottom electrodes—are required for realising STH efficiencies of  $>23\%$  in the D4 (dual light absorber: four photons to one  $H_2$ ) tandem cell. Further requirements for suitable semiconductors for PEC water splitting include a large light absorption coefficient ( $\alpha$ ), high mobility, easy processability without secondary phases, and stability to photocorrosion. In this regard, most emerging cost-competitive photoelectrode materials for PEC water splitting, such as  $TiO_2$  ( $E_g \sim 3.2$  eV)<sup>8</sup>,  $Fe_2O_3$  ( $E_g \sim 2.2$  eV)<sup>9</sup>,  $BiVO_4$  ( $E_g \sim 2.4$  eV)<sup>10</sup>, and  $Cu_2O$  ( $E_g \sim 2.0$  eV)<sup>11</sup>, are deemed unsuitable for the bottom photoelectrode due to their large  $E_g$ . Although the  $E_g$  of  $Cu_2ZnSn(S,Se)_4$  semiconductor, which is another earth-abundant material applicable for PEC water splitting, varies from 1.0 to 1.5 eV depending on the composition, the pure-phase compound suffers from severe difficulty of synthesis due to the narrow stoichiometric window<sup>12</sup>. It is worth mentioning that the secondary phase issue, i.e. the formation of undesirable detrimental phases during processing, could pose a major obstacle to large-scale commercialisation. In recent years, various low-cost semiconductors have emerged, such as  $Cu_2S$  ( $E_g \sim 1.5$  eV)<sup>13</sup>,  $CuFeO_2$  ( $E_g \sim 1.5$  eV)<sup>14</sup>,  $CuBi_2O_4$  ( $E_g \sim 1.7$  eV)<sup>15</sup>,  $CuSbS_2$  ( $E_g \sim 1.5$  eV)<sup>16</sup>, and  $SnS$  ( $E_g \sim 1.3$  eV)<sup>17</sup>. However, none of them have satisfied all the requirements for an ideal semiconductor for PEC water splitting. Therefore, a breakthrough material for realising practical STH conversion is urgently required<sup>4</sup>.

$Sb_2Se_3$  offers many advantageous properties that make it a nearly ideal semiconductor material for PEC water splitting. First, it has a small  $E_g$  of 1.1–1.2 eV. In addition, it is a low-cost semiconductor (the cost of Sb is similar to that of Cu)<sup>18</sup> and exhibits attractive optoelectronic properties ( $\alpha > 10^5$  cm<sup>-1</sup> and high mobility of  $\sim 10$  cm<sup>2</sup> V<sup>-1</sup> s<sup>-1</sup>)<sup>19,20</sup>. Moreover, the thermodynamic properties of the Sb–Se system allow only stable orthorhombic  $Sb_2Se_3$  phases without any secondary phases<sup>21</sup>, avoiding severe secondary phase issues commonly observed in other multivalent compound materials. It has also been reported that  $Sb_2Se_3$  is intrinsically stable towards photocorrosion in strong acidic media unlike  $Cu_2O$ , which is vulnerable to photocorrosion<sup>22</sup>. Owing to these merits, the photocurrent density of the  $Sb_2Se_3$  photocathode has improved rapidly from the initially reported value of 2.5 mA cm<sup>-2</sup> to 17.5 mA cm<sup>-2</sup> at 0 V against the reversible hydrogen electrode (RHE) over the short period of its development<sup>23–26</sup>. However, it is still far below the theoretical maximum (about 40 mA cm<sup>-2</sup>, assuming a 1.2 eV  $E_g$  and a 100% incident photon-to-current efficiency (IPCE)). In addition, it has been reported that the onset potential of  $Sb_2Se_3$  photocathodes can be enhanced up to 0.47 V<sub>RHE</sub><sup>27</sup>, but the photovoltage and fill factor should be further improved to realise unassisted water splitting.

As  $Sb_2Se_3$  has a one-dimensional (1D) crystal structure, it tends to grow with the morphology of 1D nanostructures, which makes

synthesis of compact  $Sb_2Se_3$  thin films difficult<sup>28</sup>. In the case wherein a light-absorbing material has a low absorption coefficient and poor electrical properties (e.g. short carrier diffusion length), 1D nanostructuring could be an attractive strategy for enhancing the performance. However, in the previously reported  $Sb_2Se_3$  photocathodes, probably owing to its good optoelectronic properties, planar-type  $Sb_2Se_3$  exhibited better performance compared with that of its elongated 1D structured counterpart<sup>24,27</sup>. One possible reason is that the incomplete coverage of  $Sb_2Se_3$  films, due to the complicated 1D morphology, can result in direct contact between the substrate and an n-type layer, which acts as a recombination centre. In addition, because the carrier transport in  $Sb_2Se_3$  along the [001] direction is more efficient than that along the [010] and [100] directions owing to its anisotropic crystallographic nature<sup>20</sup>, the p–n junction should be formed along the [001] direction to maximise the separation of the photo-generated charges. In the 1D  $Sb_2Se_3$  system, however, the p–n junction generally is formed along the [010] or [100] directions, resulting in inefficient charge separation. Thus compact film-type  $Sb_2Se_3$  with favourable crystallographic orientation for efficient charge separation (i.e. vertically aligned  $(Sb_4Se_6)_n$  nanoribbons) should be obtained to achieve high-performance  $Sb_2Se_3$  photocathodes. However, as molecular inks for  $Sb_2Se_3$  already contain 1D  $[Sb_4Se_7]^{2-}$  chains in the solution<sup>24,27</sup>, it is a daunting task to obtain compact thin  $Sb_2Se_3$  films via solution processing.

Here we report high-quality dense  $Sb_2Se_3$  thin films obtained by the close space sublimation (CSS) method, which is known to be a low-cost, large-area, high-yield deposition technique for preparing light-absorbing semiconductors, such as cadmium telluride<sup>29</sup> and  $CH_3NH_3PbI_3$ <sup>30</sup>. We implement a fast cooling strategy as well as the two-step CSS method<sup>31</sup>, enabling pin-hole-free and smooth  $Sb_2Se_3$  thin films with well-oriented  $(Sb_4Se_6)_n$  ribbons. The resulting  $Sb_2Se_3$  thin-film-based photocathodes reveal a highest photocurrent density close to 30 mA cm<sup>-2</sup> at 0 V<sub>RHE</sub>. The performance of the newly developed  $Sb_2Se_3$  photocathode is utilised by unassisted overall water splitting PEC cells after judiciously optimising the photovoltage and electrolyte compatibility to the  $BiVO_4$  photoanode. The D4 tandem cell of  $Sb_2Se_3$ – $BiVO_4$  in a neutral phosphate buffer successfully demonstrates an impressive STH efficiency of 1.5% with 10 h of stability. Realisation of the  $Sb_2Se_3$ -based tandem device, capable of harvesting a broad range of photons with the readily obtained earth-abundant semiconductor, allows us to envision practical solar hydrogen production via efficient and cost-competitive PEC water splitting.

## Results

**Fabrication of compact and well-oriented  $Sb_2Se_3$  thin films.** In order to avoid the formation of the thermodynamically favourable 1D structure as well as induce the metastable thin film morphology of  $Sb_2Se_3$ , we tried to kinetically suppress the rearrangement of  $(Sb_4Se_6)_n$  nanoribbons by employing a two-step deposition where a low-temperature (340 °C) seed layer was deposited prior to the high-temperature (460 °C) deposition<sup>31</sup>. In general, the CSS system employs one-step deposition at a high temperature (e.g. 400–550 °C for CdTe) to achieve a suitable growth rate<sup>29</sup>. Owing to the highly anisotropic nature of  $Sb_2Se_3$ , however, the low-temperature deposition is an imperative step to obtain a compact morphology. At the first deposition step of 340 °C, a compact thin film could be obtained, whereas an elongated 1D structure with incomplete coverage was observed when a temperature of 460 °C was applied directly (Supplementary Fig. 1). Figure 1a–c show the microstructures of  $Sb_2Se_3$  thin films deposited on an Au/fluorine-doped tin oxide (FTO) substrate by the two-step CSS deposition process (i.e. successive depositions at 340 and 460 °C followed by cooling the chamber

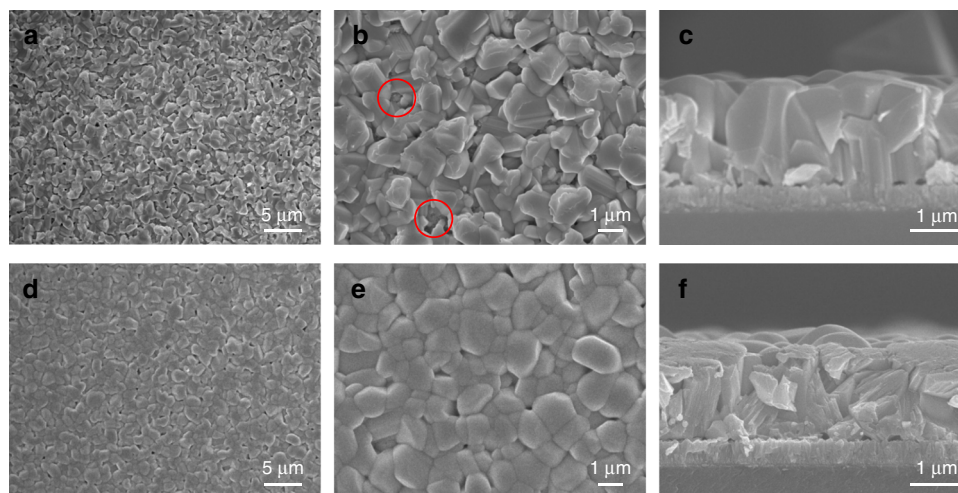


**Fig. 1** Microstructures and crystallographic orientation of  $\text{Sb}_2\text{Se}_3$  thin films. **a–c** SEM images of **a–c** slow-cooling  $\text{Sb}_2\text{Se}_3$  and **d–f** fast-cooling  $\text{Sb}_2\text{Se}_3$ .

naturally after deposition). The role of the Au layer in  $\text{Sb}_2\text{Se}_3$  photoelectrodes, which facilitates the transfer of photo-generated holes, has been discussed in previous reports on  $\text{Sb}_2\text{Se}_3$  for PEC water splitting<sup>26,32</sup> and thin-film solar cells<sup>33</sup>. Despite the film-type morphology, there were some pin-holes resulting in exposure of the substrate (red circles in Fig. 1b) with the faceted morphology of the  $\text{Sb}_2\text{Se}_3$  thin films. Interestingly, it was found that a much smoother pin-hole-free surface was achieved when  $\text{N}_2$  gas was passed during the cooling process after deposition under the same conditions (i.e. successive depositions at 350 and 450 °C), as shown in Fig. 1d–f. We denoted the sample prepared with  $\text{N}_2$ -assisted cooling as the ‘fast-cooling’ sample, while the naturally cooled sample was denoted as the ‘slow-cooling’ sample. The cooling rates for the fast cooling and the slow cooling until it has reached 200 °C are approximately 15.7 and 11.3 °C min<sup>-1</sup>, respectively. The detailed differences between the two samples, including grain size distribution and crystallographic orientations, are shown in Supplementary Figs. 2–4.

On comparing the morphological and crystallographic differences between the fast- and slow-cooling samples, it was obvious that the  $\text{N}_2$  flow during the cooling process significantly affects the morphology and crystallographic orientation. As mentioned above, because  $\text{Sb}_2\text{Se}_3$  has a strong 1D anisotropic nature, thermodynamically favourable sharp and facet morphologies are inevitably obtained when kinetically sufficient time is provided (i.e. slow cooling). In contrast, in case of fast cooling, which offers insufficient time to reach the thermodynamically stable morphology, a metastable smooth morphology can be achieved. This explanation is supported by the solution-processed  $\text{Sb}_2\text{Se}_3$ , in which 1D nanostructures were observed when sufficient Se precursor was provided, while the metastable planar-type  $\text{Sb}_2\text{Se}_3$  was obtained in Se-deficient conditions<sup>27</sup>. In addition, a slight change in X-ray diffraction (XRD) data implied that the ribbons likely move during the cooling process, presumably due to the low melting temperature of  $\text{Sb}_2\text{Se}_3$  (~608 °C). Thus it can be reasonably concluded that, in order to fabricate compact thin-film-type  $\text{Sb}_2\text{Se}_3$  with favourably oriented  $(\text{Sb}_4\text{Se}_6)_n$  ribbons, rearrangement of the ribbons should be kinetically suppressed as much as possible to prevent the formation of thermodynamically stable 1D structures. Obtained with kinetically controlled growth, it was possible to obtain  $\text{Sb}_2\text{Se}_3$  thin films with a compact structure as well as well-oriented ribbons, both of which are expected to be favourable for better performance.

**PEC performance of CSS- $\text{Sb}_2\text{Se}_3$  photocathodes.** Figure 2a, b show the PEC performance of  $\text{RuO}_x/\text{TiO}_2/\text{Sb}_2\text{Se}_3/\text{Au}/\text{FTO}$  photocathodes using fast- and slow-cooling  $\text{Sb}_2\text{Se}_3$  films measured in pH 1 electrolytes. As we mentioned above, the Au layer acts as a hole-selective contact, which facilitates the transfer of photo-generated holes while blocking the electrons backflow<sup>32,33</sup>. Without the Au layer,  $\text{Sb}_2\text{Se}_3$  photocathodes revealed relatively poor performance while nearly similar morphology of  $\text{Sb}_2\text{Se}_3$  was observed (Supplementary Fig. 5), which verifies the role of the Au layer not affecting the growth of  $\text{Sb}_2\text{Se}_3$  but assisting the transfer of photo-generated charges. The  $\text{RuO}_x$  catalytic layer was deposited by the PEC method, while atomic layer deposition (ALD) was used for the  $\text{TiO}_2$  layer, similar to a previous study<sup>32</sup>. In both samples, the onset potentials shifted towards a positive direction after the first scan due to activation of the  $\text{RuO}_x$  catalyst<sup>34</sup>. The photocurrent density of the fast-cooling sample approached 30 mA cm<sup>-2</sup> at 0  $V_{\text{RHE}}$ , which is not only the highest value obtained for a  $\text{Sb}_2\text{Se}_3$  photocathode but also among the best observed for all photoelectrodes used in PEC water splitting so far. Note that the data shown in Fig. 2 were obtained from the best-performing device, while normally 25–30 cm<sup>-2</sup> at 0  $V_{\text{RHE}}$  photocurrent density was observed in the fast-cooling  $\text{Sb}_2\text{Se}_3$ -based photocathodes. The previously reported photocurrent densities of photoelectrodes for PEC water splitting are shown in Supplementary Fig. 6. Given the low-cost and relatively short history of  $\text{Sb}_2\text{Se}_3$  as well as the simple preparation and low material usage due to the high  $\alpha$ , the high photocurrent density of ~30 mA cm<sup>-2</sup> at 0  $V_{\text{RHE}}$  clearly demonstrates the strong potential of  $\text{Sb}_2\text{Se}_3$  as a promising photocathode material.

While the fast-cooling sample revealed a record photocurrent density, the photocurrent density of the slow-cooling sample with a  $\text{RuO}_x$  co-catalyst, which had a facet morphology, was relatively low (~17 mA cm<sup>-2</sup> at 0  $V_{\text{RHE}}$ , Fig. 2b). Figure 2c exhibits the half-cell STH conversion efficiencies (HC-STH) calculated from the third scans in Fig. 2a, b according to the equation  $\text{HC-STH} = I_{\text{ph}} \times (E_{\text{RHE}} - E_{\text{H}^+/\text{H}_2}) / P_{\text{SUN}} \times 100\%$ , where  $I_{\text{ph}}$  is the photocurrent density obtained under an applied bias of  $E_{\text{RHE}}$ ,  $E_{\text{H}^+/\text{H}_2}$  is 0  $V_{\text{RHE}}$ , and  $P_{\text{SUN}}$  is 100 mW cm<sup>-2</sup>. It is worth noting that the maximum value of HC-STH in the fast cooling was observed at a more positive potential of 0.16  $V_{\text{RHE}}$  compared with that of the slow-cooling counterpart (0.09  $V_{\text{RHE}}$ ), indicating that the fast-cooling strategy is advantageous for not only the photocurrent but also the photovoltage and fill factor. As shown in Fig. 2d, both fast- and

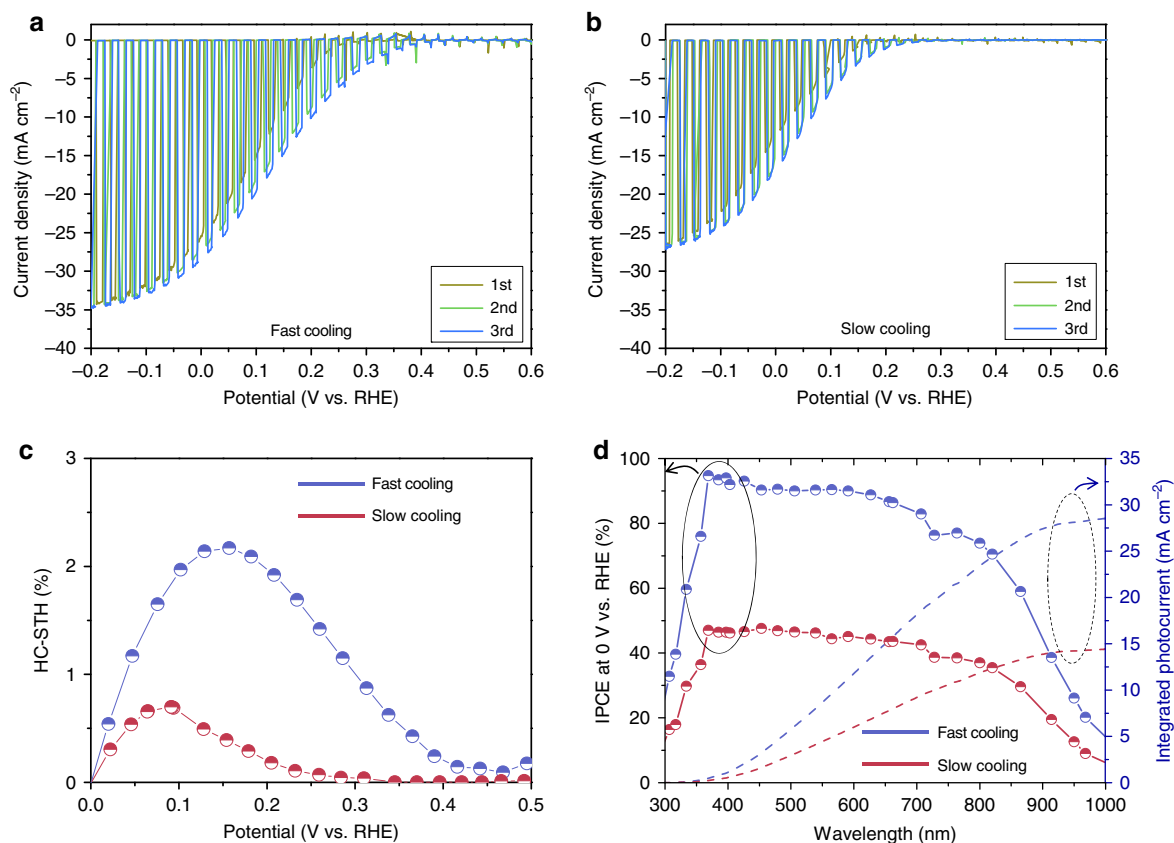


**Fig. 2** PEC performance of  $\text{RuO}_x/\text{TiO}_2/\text{Sb}_2\text{Se}_3/\text{Au}/\text{FTO}$  photocathodes in pH 1  $\text{H}_2\text{SO}_4$  electrolyte. **a, b**  $J$ - $V$  curves of **a** fast- and **b** slow-cooling samples under simulated 1 sun air mass 1.5 G chopped illumination at a scan speed of  $5 \text{ mV s}^{-1}$  from positive to negative potential and **c** corresponding HC-STH efficiencies. **d** Wavelength-dependent IPCE and integrated photocurrent density of fast- and slow-cooling samples measured at  $0 \text{ V}_{\text{RHE}}$ . Source data used to generate this figure can be found in the Source Data file.

slow-cooling  $\text{Sb}_2\text{Se}_3$  photocathodes were able to harvest photons over 1000 nm, but the IPEC was much higher for the fast-cooling sample over the entire wavelength. Because the optical properties (e.g. surface reflection of  $\text{Sb}_2\text{Se}_3/\text{Au}/\text{FTO}$  samples) for the fast- and slow-cooling samples were nearly identical (Supplementary Fig. 7), optical properties can be excluded from the potential origin of the difference noted in the performance. In addition, a similar performance was observed when a Pt co-catalyst was used ( $\text{Pt}/\text{TiO}_2/\text{Sb}_2\text{Se}_3/\text{Au}/\text{FTO}$ , Supplementary Fig. 8): thus we can conclude that the performance difference arose not from the co-catalyst but presumably from the  $\text{TiO}_2/\text{Sb}_2\text{Se}_3$  junction.

In order to understand the performance difference observed for the fast- and slow-cooling samples, we performed Kelvin probe force microscopy (KPFM) analyses, which allowed us to investigate the topography and surface potential distribution. Figure 3a, c and b, d show the surface topography and surface potential of  $\text{TiO}_2/\text{Sb}_2\text{Se}_3$  devices, respectively. The fast-cooling  $\text{TiO}_2/\text{Sb}_2\text{Se}_3$  revealed relatively uniform distribution of surface topography and potential, as shown in Fig. 3a, b. On the other hand, some noticeable high-potential regions, as represented by the bright yellow colour in Fig. 3d, were observed for the slow-cooling  $\text{TiO}_2/\text{Sb}_2\text{Se}_3$  sample. Topography and potential line profiling for the fast-cooling sample suggested that the potential resembles the topography of  $\text{TiO}_2/\text{Sb}_2\text{Se}_3$  (Fig. 3e), indicating a lower surface potential at the grain boundaries of  $\text{Sb}_2\text{Se}_3$ <sup>35</sup>. In the fast-cooling sample, the separation of the photo-generated electrons and holes efficiently occurred along the vertically aligned  $[\text{Sb}_4\text{Se}_6]_n$  ribbons, as shown in Fig. 3g, owing to the p-n junction and relatively small lateral potential difference. In contrast, in the slow-cooling sample, the surface potential increased significantly with a rapid drop in the topography (Fig. 3f),

indicating direct contact between the n-type  $\text{TiO}_2$  layer and substrate due to pin-holes. It might be worth to note that the height recorded by AFM and KPFM ranged from a few nm to hundreds nm and even sometimes  $\mu\text{m}$  scale<sup>36,37</sup>. In such a case, the photo-excited electrons can be extracted laterally to the ribbons and they can recombine with the holes at the back contact as shown in Fig. 3h due to the large electric field across the p-n junction. It is widely known that direct contact between the top and bottom contact (i.e., in this case, the  $\text{TiO}_2$  and Au layers) can cause significant degradation of the performance, even in the case of the chemical composition and optoelectronic properties have negligible differences. For example, Luo et al. reported the effect of a thin blocking layer to prevent shunt pathways, thereby enabling much higher performance in  $\text{Cu}_2\text{O}$  nanowire photocathodes without any noticeable differences in chemical composition and morphology<sup>38</sup>. The KPFM results clearly demonstrated the importance of pin-hole-free compact thin films in preventing the recombination and the performance degradation mechanism in the presence of pin-holes, which had not yet been experimentally demonstrated.

**$\text{Sb}_2\text{Se}_3$  photocathodes in unassisted water splitting.** Despite the high photocurrent density of the fast-cooling CSS- $\text{Sb}_2\text{Se}_3$  photocathodes, there remain some issues prior to achieving unassisted water splitting by fabricating a tandem device in conjunction with the photoanode. After the optimisation of the electrolyte and the onset potential (Supplementary Figs. 9–11), we decided to use a Pt co-catalyst for the PEC tandem device. With the Pt co-catalyst, we inserted a CdS layer between  $\text{TiO}_2$  and the fast-cooling  $\text{Sb}_2\text{Se}_3$  to further enhance the onset potential, as shown in Fig. 4a<sup>27</sup>. The

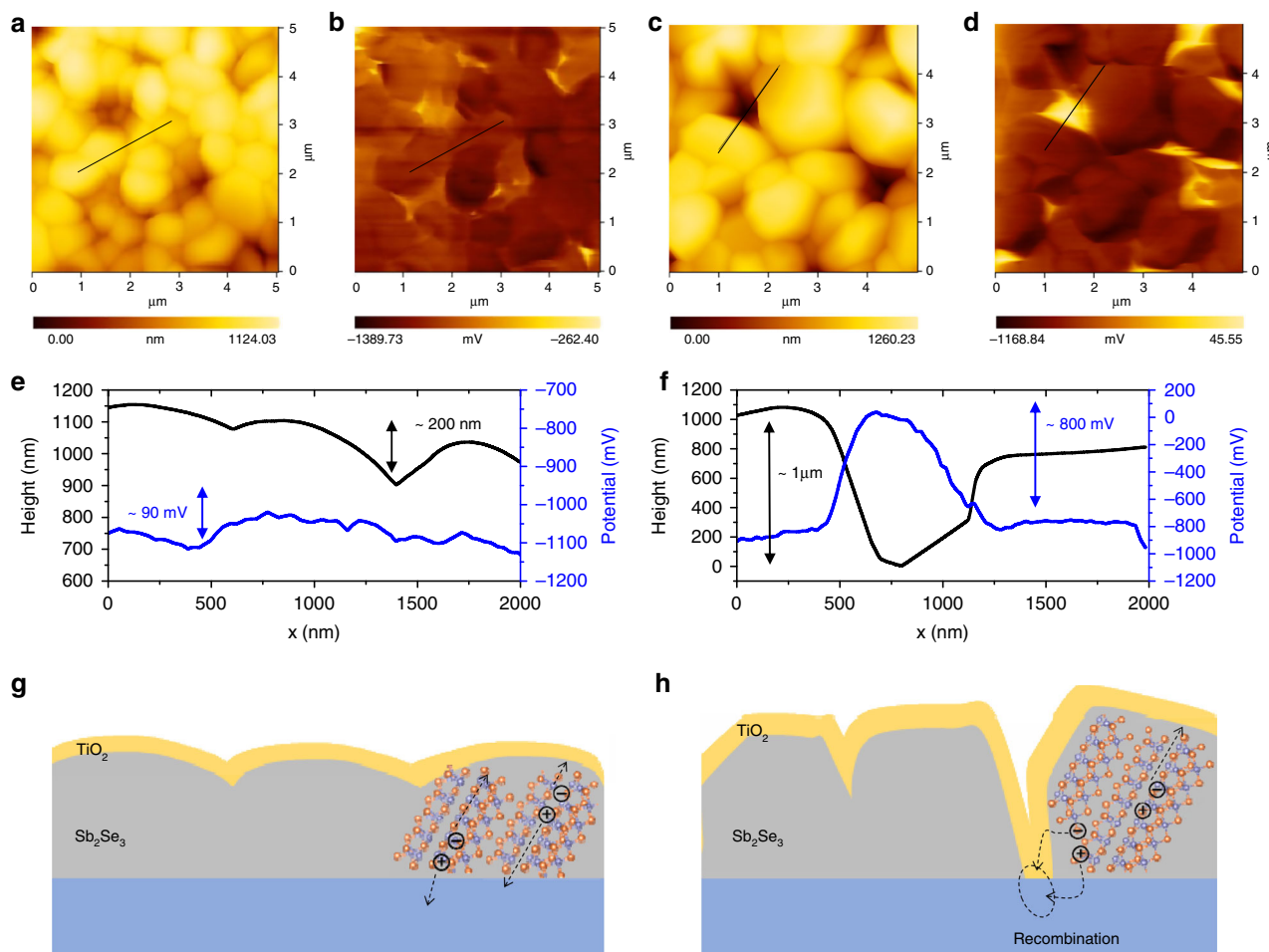


**Fig. 3 Topography and surface potential of  $\text{TiO}_2/\text{Sb}_2\text{Se}_3$  according to KPFM analysis.** **a, c** Topography of **a** fast- and **c** slow-cooling samples. **b, d** Surface potential of **b** fast- and **d** slow-cooling samples. **e, f** Topography and potential line profile (obtained from scanning the black lines in Fig. 3a-d) for **e** fast- and **f** slow-cooling samples. **g, h** Schematics showing possible charge separation and recombination in **g** fast- and **h** slow-cooling samples. Source data used to generate this figure can be found in the Source Data file.

thickness of the CdS and  $\text{TiO}_2$  layers were approximately 50 and 30 nm, respectively (Supplementary Fig. 12). Upon deposition of the CdS layer, the onset potential of the  $\text{Sb}_2\text{Se}_3$  photocathode shifted up to  $0.5 V_{\text{RHE}}$  and the fill factor was also significantly enhanced (Fig. 4b). As a result, the maximum HC-STH increased from 2.33% to 3.4%, and the potential at which the maximum HC-STH was observed also shifted from 0.18 to  $0.26 V_{\text{RHE}}$ , as shown in Fig. 4c. Therefore, despite the slightly decreased photocurrent density at  $0 V_{\text{RHE}}$ , Pt/ $\text{TiO}_2$ /CdS/ $\text{Sb}_2\text{Se}_3$  configuration was more suitable for the PEC tandem device. The enhanced onset potential and fill factor could be attributed to the reduced band mismatch between  $\text{TiO}_2$  and  $\text{Sb}_2\text{Se}_3$ <sup>27</sup>. Figure 4d shows the IPCE spectra for  $\text{Sb}_2\text{Se}_3$  photocathodes with and without CdS layers, suggesting that the IPEC of 300–500 nm decreased with the thickness of the CdS layer. The reduced IPCE values imply that the photons absorbed by the CdS ( $E_g \sim 2.4$  eV,  $\sim 516.6$  nm) were unable to contribute to the photocurrent density. Therefore, when the thickness of the CdS layer increased, the photocurrent density decreased, whereas the onset potential remained the same (i.e.  $\sim 0.5 V_{\text{RHE}}$ ), indicating the necessity of careful optimisation of the CdS layer thickness (Supplementary Fig. 13).

**D4 tandem cell for unbiased solar overall water splitting.** Since the band gap of  $\text{Sb}_2\text{Se}_3$  is 1.2 eV, which is suitable for realising a D4 tandem cell as a bottom electrode with a different top light

absorber<sup>39</sup>, we fabricated tandem cells coupled with  $\text{BiVO}_4$ -based photoanodes ( $E_g \sim 2.4$  eV), which have been widely used for high-performance photocathode–photoanode tandem cells<sup>10</sup> (Fig. 5a). The H,Mo:BiVO<sub>4</sub> photoanode used here revealed good transparency (Supplementary Fig. 14) and performance ( $\sim 4.7 \text{ mA cm}^{-2}$  at  $1.23 V_{\text{RHE}}$  and onset potential of  $0.25\text{--}0.3 V_{\text{RHE}}$ ) as a top light absorber. To achieve high efficiency, further optimisation of the electrolyte was conducted for the tandem cell comprising two photoelectrodes involving opposite reactions (Supplementary Figs. 15–18).

As shown in Fig. 5b, the operating point of the two photoelectrodes, as estimated by the intersection of two  $J$ - $V$  curves, was approximately  $1.2 \text{ mA cm}^{-2}$  at  $0.4 V_{\text{RHE}}$ , which corresponded to a STH efficiency of 1.5%. It should be noted that photocurrent density of  $\text{BiVO}_4$  at  $0.4 V_{\text{RHE}}$  varies from 1.2 to  $0.8 \text{ mA cm}^{-2}$ , thus the overall STH efficiencies of the tandem cell range from 1.48% to 0.98%. In addition, the polarisation curves of  $\text{BiVO}_4$ -Pt (as the counter electrode) and  $\text{BiVO}_4$ - $\text{Sb}_2\text{Se}_3$  (as the counter electrode) demonstrated a  $\sim 0.5$  V anodic shift induced by the  $\text{Sb}_2\text{Se}_3$  photocathode, indicating that the  $\text{Sb}_2\text{Se}_3$  photocathode provided a photovoltage of 0.5 V (Fig. 5c). The  $\text{BiVO}_4$ - $\text{Sb}_2\text{Se}_3$  tandem cell exhibited  $1.2 \text{ mA cm}^{-2}$  at 0 V against the counter electrode (i.e. unbiased conditions), which was in agreement with the estimated value according to the overlapped  $J$ - $V$  curves shown in Fig. 5b. This observation verified that the total photovoltage of 1.45 V (0.52 V from the  $\text{Sb}_2\text{Se}_3$  photocathode

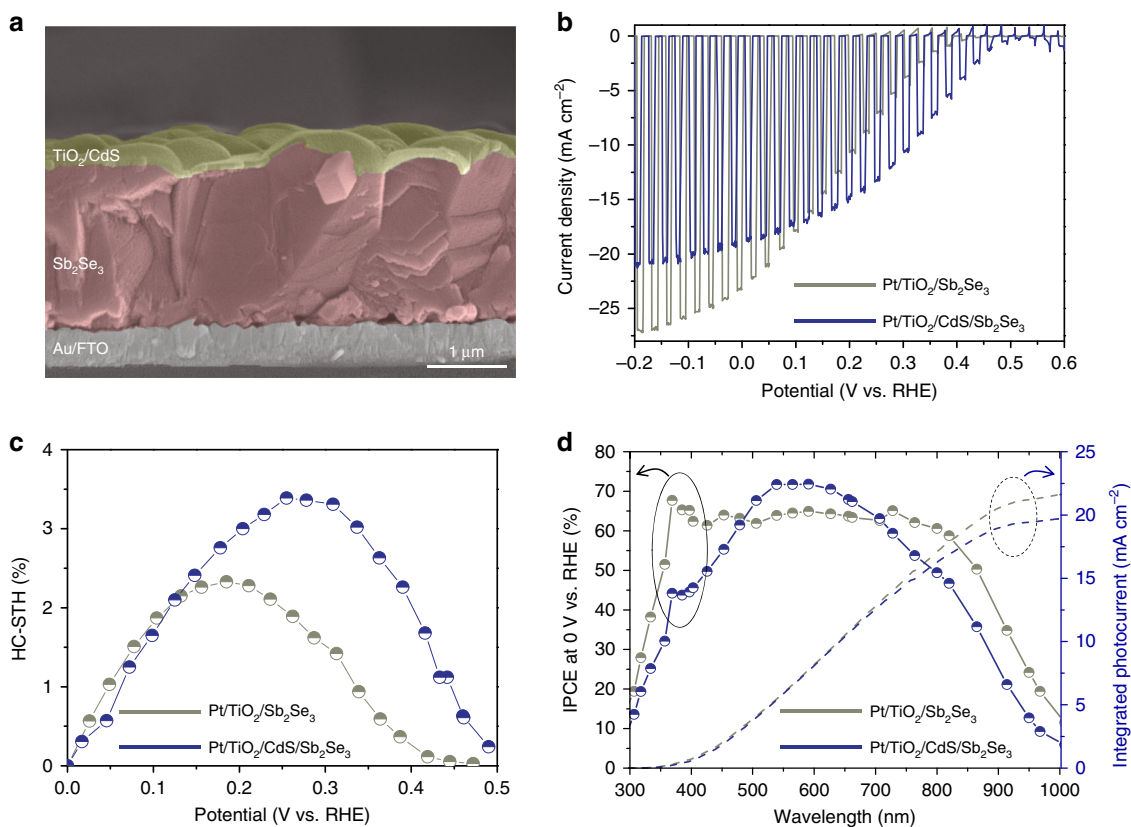


**Fig. 4** Microstructure and PEC performance of Pt/TiO<sub>2</sub>/CdS/Sb<sub>2</sub>Se<sub>3</sub>/Au/FTO photocathodes. **a** Cross-sectional SEM image of TiO<sub>2</sub>/CdS/Sb<sub>2</sub>Se<sub>3</sub> on Au/FTO substrate. **b** *J*-*V* curves for Sb<sub>2</sub>Se<sub>3</sub> photocathodes with/without a CdS layer in pH 1 H<sub>2</sub>SO<sub>4</sub> under simulated 1 sun air mass 1.5 G chopped illumination at a scan speed of 5 mV s<sup>-1</sup> from positive to negative potential and **c** corresponding HC-STH efficiencies. **d** Wavelength-dependent IPCE at 0 V<sub>RHE</sub> of Sb<sub>2</sub>Se<sub>3</sub> photocathodes with/without CdS layer. Source data used to generate this figure can be found in the Source Data file.

and 0.93 V from the BiVO<sub>4</sub> photoanode) was sufficient to implement unbiased overall water splitting, resulting in evolution of both H<sub>2</sub> and O<sub>2</sub>, by overcoming the thermodynamic potential requirement (1.23 V). In comparison to previously reported photoelectrodes, the total photovoltage of 1.45 V was a moderate value considering the band gap energies<sup>40</sup>. Thus it is noteworthy that a photovoltage increment of ~0.1 V and the enhanced fill factor obtained using CdS played a critical role in driving the overall water splitting.

Photon utilisation capability of the BiVO<sub>4</sub>-Sb<sub>2</sub>Se<sub>3</sub> tandem cell was confirmed by IPCE measurements. For BiVO<sub>4</sub>, photons up to ~510 nm (*E<sub>g</sub>* of 2.45 eV) could be converted and the absorption current density, which represents the maximum photocurrent density under the absorbance of BiVO<sub>4</sub>, was calculated to be 5.5 mA cm<sup>-2</sup> (Supplementary Fig. 14b). Sum of the photon flux before and after passing through BiVO<sub>4</sub> up to the wavelength of 1033 nm (~1.2 eV, *E<sub>g</sub>* of Sb<sub>2</sub>Se<sub>3</sub>) was calculated to be 39.9 and 24.4 mA cm<sup>-2</sup>, respectively, which are much higher than the photocurrent of BiVO<sub>4</sub> at the top of the tandem cell configuration.

We compared BiVO<sub>4</sub> and Sb<sub>2</sub>Se<sub>3</sub> in two different bias conditions: high bias near short circuit of the individual photoelectrode (1.0 V<sub>RHE</sub> for photoanode and 0.1 V<sub>RHE</sub> for photocathode; Supplementary Fig. 19) and operating bias at ‘actual’ operating point (0.4 V<sub>RHE</sub> for both the photocathode and photoanode; Fig. 5d). In both cases, a broad range of photons could be effectively utilised by the synergetic effect of BiVO<sub>4</sub> (to 510 nm) and Sb<sub>2</sub>Se<sub>3</sub> (from 450 to 1000 nm). In case of the high bias condition, both the photocathode and photoanode showed a quite high IPCE (~70% at 450 nm for BiVO<sub>4</sub> and ~60%

for Sb<sub>2</sub>Se<sub>3</sub>). The photocurrent calculated from the IPCE was 3.2 mA cm<sup>-2</sup> for the BiVO<sub>4</sub> photoanode. In addition, the photocurrent of the Sb<sub>2</sub>Se<sub>3</sub> photocathodes was 18.5 and 10.3 mA cm<sup>-2</sup> with or without BiVO<sub>4</sub>, respectively. These values are in a good agreement with photocurrents shown in the *J*-*V* curves (Supplementary Fig. 18). On the other hand, as expected, a lower IPCE was observed under the operating bias (0.4 V<sub>RHE</sub>): ~25% at 450 nm for BiVO<sub>4</sub> and ~15% for Sb<sub>2</sub>Se<sub>3</sub>, as shown in Fig. 5d. The photocurrent density calculated using the IPCE spectra of BiVO<sub>4</sub> at 0.4 V<sub>RHE</sub> was about 1.1 mA cm<sup>-2</sup>, which is similar to the values shown by the *J*-*V* curve (Supplementary Fig. 18). However, the photocurrent density of Sb<sub>2</sub>Se<sub>3</sub> photocathodes at 0.4 V<sub>RHE</sub> with and without BiVO<sub>4</sub> were 5.0 and 2.2 mA cm<sup>-2</sup>, respectively, which are higher than the photocurrents shown by the *J*-*V* curve. This discrepancy between the photocurrent density at 0.4 V<sub>RHE</sub> demonstrated by the IPCE and *J*-*V* curve can be attributed to the light-intensity-dependent carrier mobility of Sb<sub>2</sub>Se<sub>3</sub>. As the carrier mobility of Sb<sub>2</sub>Se<sub>3</sub> is much higher under low-intensity light<sup>32</sup>, Sb<sub>2</sub>Se<sub>3</sub> photocathodes showed a better fill factor in IPCE measurement conditions (~100 μW cm<sup>-2</sup>) compared with the 1 sun conditions (100 mW cm<sup>-2</sup>), thereby resulting in a higher photocurrent according to the IPCE spectra at 0.4 V<sub>RHE</sub>. The D4 tandem cell consisting of Sb<sub>2</sub>Se<sub>3</sub> and BiVO<sub>4</sub> operated stably for over 10 h without any noticeable degradation in the photocurrent density (Fig. 5e). The efficiency and stability of our Sb<sub>2</sub>Se<sub>3</sub>-based tandem cells are comparable to those of the best-performing tandem cells containing other types of photocathode materials (vide infra). Finally, a larger tandem cell was constructed using a BiVO<sub>4</sub> photoanode (0.81 cm<sup>-2</sup>) and a Sb<sub>2</sub>Se<sub>3</sub> photocathode (0.35 cm<sup>-2</sup>)

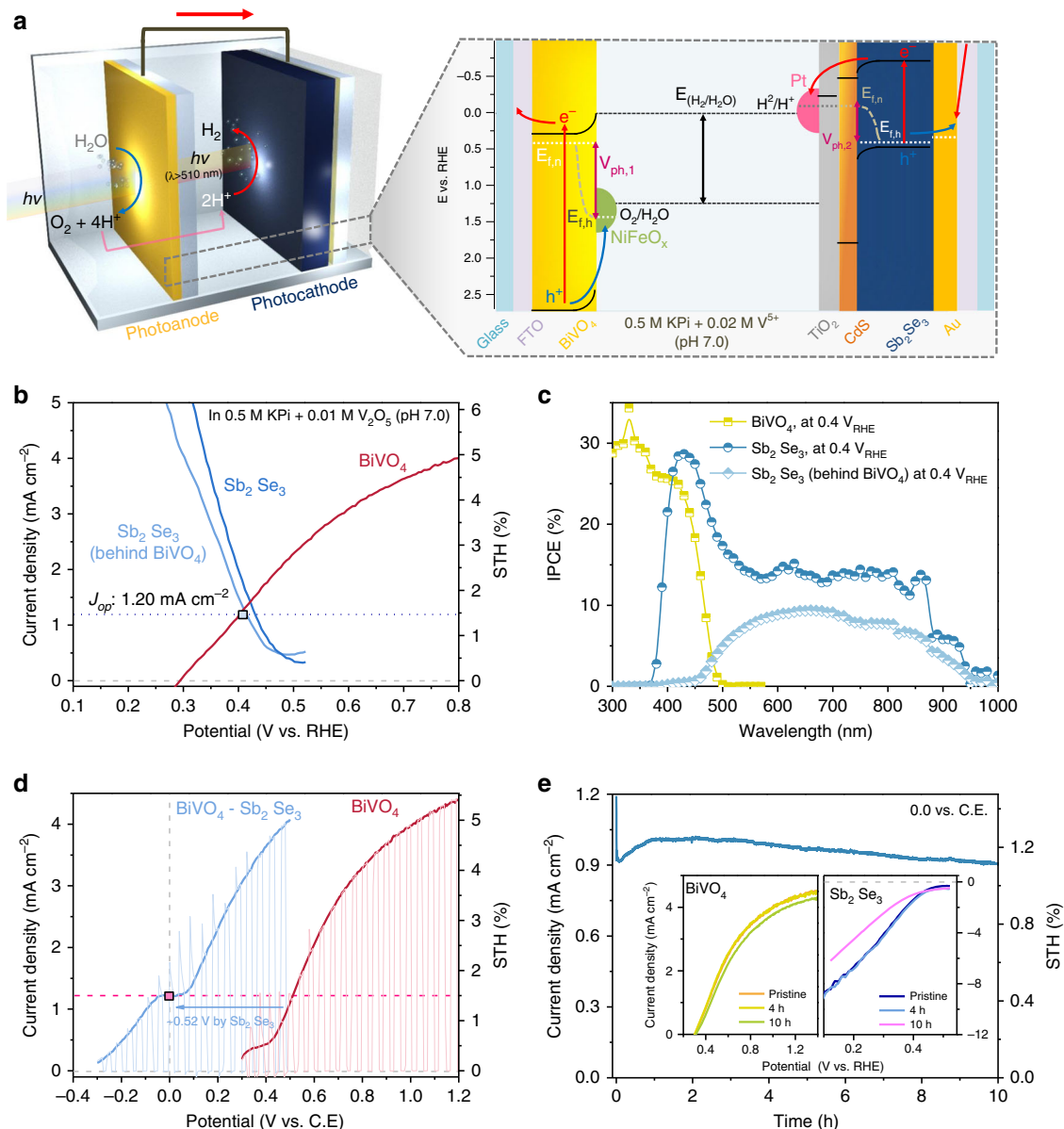


**Fig. 5** Sb<sub>2</sub>Se<sub>3</sub> photocathode-BiVO<sub>4</sub> photoanode for solar overall water splitting PEC cell. **a** Scheme of the NiFeO<sub>x</sub>/H<sub>2</sub>Mo:BiVO<sub>4</sub>/FTO-Pt/TiO<sub>2</sub>/CdS/Sb<sub>2</sub>Se<sub>3</sub>/Au/FTO tandem cell operating in pH 7.0 phosphate buffer. **b** J-V curve for the photocathode and photoanode; the operating point is marked for the tandem cell (photoelectrode active area: 0.32 cm<sup>2</sup>). **c** Two-electrode measurements for photoanode-counter electrode (C. E.) and photoanode-photocathode tandem cells (active area: 0.28 cm<sup>2</sup>). **d** IPCE at 0.4 V<sub>RHE</sub> measured for the photoanode and photocathodes. **e** Photocurrent generation under short circuit conditions (0 against counter electrode) of the photoanode-photocathode tandem cell. All analyses were conducted in 0.5 M phosphate buffer + 0.01 M V<sub>2</sub>O<sub>5</sub> (pH 7.0) at a scan rate of 20 mV s<sup>-1</sup>. Distance between the photoanode and photocathode was ~0.5 cm. Source data used to generate this figure can be found in the Source Data file.

under simulated ~3 sun, which clearly demonstrated a constant generation of O<sub>2</sub> and H<sub>2</sub> gas evolution (Supplementary video 1, Supplementary Fig. 20).

## Discussion

Even though we report herein the first demonstration of unbiased water splitting using a Sb<sub>2</sub>Se<sub>3</sub> photocathode in a single reactor, better tandem cell systems are likely achievable by using two different electrolytes that are separately optimised for each photoelectrode (e.g. pH 1 for Sb<sub>2</sub>Se<sub>3</sub> and pH 9 borate for BiVO<sub>4</sub>) along with a bipolar membrane<sup>41</sup> or stabilising both the photocathode and photoanode using additives (e.g. chelating agent to deter poisoning) in the electrolyte<sup>42</sup>. Bearing in mind its short history

and potential for further enhancement, the performance of the Sb<sub>2</sub>Se<sub>3</sub>-based tandem cell (STH efficiency of 1.5% and stability of over 10 h) is quite remarkable particularly in comparison with previously reported results for photocathode-photoanode tandem cells<sup>4</sup> (Fig. 6a, Table 1 in Supplementary Information). We categorised the tandem cells based on the bottom light absorbers (silicon based, III-V, Cu-chalcogenides, metal oxides, and perovskites). Most of them used BiVO<sub>4</sub>, which is currently the most suitable photoanode material and ensures good transparency (~80% beyond photon utilisation threshold (~520 nm))<sup>10</sup>. It was found that the efficiency of the BiVO<sub>4</sub>-Sb<sub>2</sub>Se<sub>3</sub> tandem cell (1.5% STH) was not the highest when compared to that of BiVO<sub>4</sub>-CIGS (3.7%)<sup>43</sup>, BiVO<sub>4</sub>-Cu<sub>2</sub>O (3.0%)<sup>44</sup>, and BiVO<sub>4</sub>-c-Si (2.1%)<sup>41</sup>. Considering the cost of materials (much lower than that of CIGS),

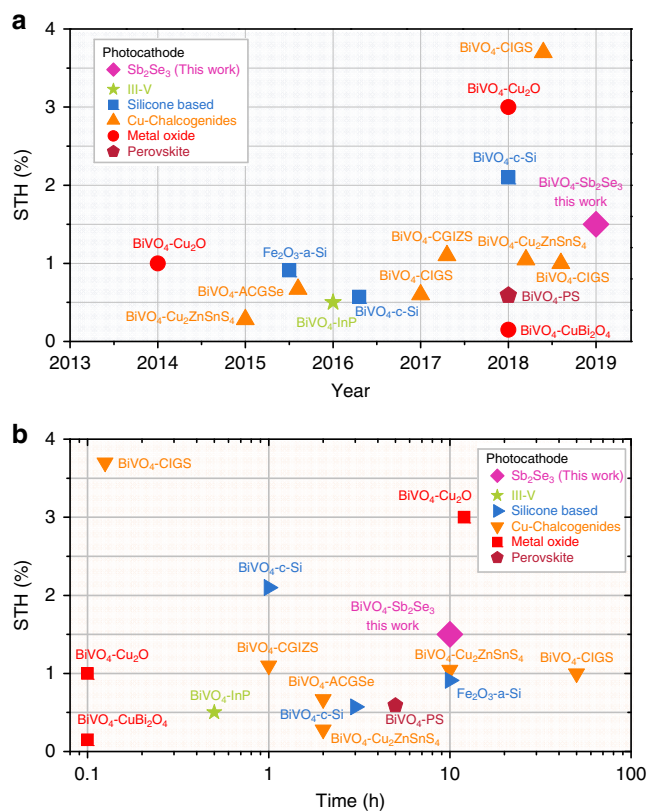


**Fig. 6 Efficiency and stability benchmarks for photoanode-photocathode D4 tandem cell. a** Solar-to-hydrogen efficiencies reported in recent years and **b** their operation duration. All reports are summarised in Supplementary Table 1.

small band gap (compared to that of Cu<sub>2</sub>O,  $E_g \sim 2.0$  eV), simple preparation, and low material usage (compared to that of Czochralski-grown Si wafer and complicated Si microwires), the >1% STH can be considered a significant milestone for PEC tandem cells. Moreover, 10 h of stability is also the best result reported for photoanode-photocathode tandem cells except for the 20 h stability achieved by the expensive CIGS-based photocathodes<sup>45</sup> (Fig. 6b). The exceptional performance and stability of the Sb<sub>2</sub>Se<sub>3</sub> photocathode presented here, as well as several desirable material characteristics of Sb<sub>2</sub>Se<sub>3</sub> such as its high  $\alpha$ , optimal band gap of  $\sim 1.2$  eV, and comparable photovoltage to that of c-Si ( $\sim 0.5$  V), clearly present a promising pathway towards realising a competitive overall water splitting PEC cell system, which could potentially result in an STH of approximately 10% using BiVO<sub>4</sub> photoanodes whose  $E_g$  is 2.4 eV (Supplementary Fig. 21a). In order to demonstrate a higher STH efficiency, the areas of focus should include enhancing both the photovoltage and fill factor through interface engineering, such as the recently reported dipole engineering at the buried junction<sup>46</sup>. In addition, the development of an ideal photoanode material with an  $E_g$  close to 1.8 eV could potentially enable an STH efficiency of >20% on using the Sb<sub>2</sub>Se<sub>3</sub> photocathode (Supplementary Fig. 21b). Although the value of STH 1.5% is not superior in comparison to that of other systems, such as photovoltaic-electrolytic systems (average 10–20%), buried-junction photoelectrodes (10–15%), and photovoltaic-PEC systems (3–8%), because of the simplicity of the photoanode-photocathode system, the price of hydrogen produced from such a system will be lower. Therefore, not only the STH efficiency but also the cost should be considered when comparing such systems. The reported STH efficiencies of the photoanode-photocathode

tandem system are increasing very rapidly (Fig. 6), which suggests increasing research interest in reducing the complexity of overall water splitting devices<sup>4</sup>.

In summary, we have demonstrated a high-performance photocathode using a low-cost Sb<sub>2</sub>Se<sub>3</sub> semiconductor, which has a small  $E_g$  ( $\sim 1.2$  eV), good optoelectronic properties, and no secondary phase. By suppressing the growth kinetics during the CSS deposition, a compact and pinhole-free Sb<sub>2</sub>Se<sub>3</sub> thin film was obtained, which enabled a highest photocurrent density of up to 30 mA cm<sup>-2</sup> by avoiding recombination and accelerating charge separation through well-aligned (Sb<sub>4</sub>Se<sub>6</sub>)<sub>n</sub> ribbons. Inserting a CdS layer between Sb<sub>2</sub>Se<sub>3</sub> and TiO<sub>2</sub> increased the onset potential and consequently improved the HC-STH efficiency up to 3.4%. Finally, by combining the material with a BiVO<sub>4</sub> photoanode, unbiased overall water splitting was achieved with impressive efficiency ( $\sim 1.5\%$ ) and high stability of 10 h. These performances and stability significantly surpass those of previously reported Sb<sub>2</sub>Se<sub>3</sub> photocathodes and are comparable to those of other expensive thin film photocathodes. Given the relatively short history of photoelectric materials, it is expected that rapid progress of Sb<sub>2</sub>Se<sub>3</sub> photocathodes will lead to better efficiency in the near future and our findings represent an important demonstration of a photocathode-photoanode-based PEC device. We believe that the emerging Sb<sub>2</sub>Se<sub>3</sub> substrate can be an attractive breakthrough material for practical solar fuel production.

## Methods

**Preparation of Sb<sub>2</sub>Se<sub>3</sub> thin films.** Sb<sub>2</sub>Se<sub>3</sub> films were deposited via a two-step CSS process<sup>31</sup> using a custom-made CSS system. First, a compact layer was grown from stoichiometric Sb<sub>2</sub>Se<sub>3</sub> (Alfa Aesar, 99.999% metals basis) using a source temperature of 340 °C and a substrate temperature of 390 °C for 2 min at a pressure of 0.05 mbar. Subsequently, deposition was completed using a source temperature of 460 °C for 15 min and a pressure of 13 mbar. These films were then cooled either slowly or fast, by turning the heater off and flowing N<sub>2</sub> over the sample at a rate of either 0 or 5 L min<sup>-1</sup>, respectively.

**Deposition of overlayers and catalysts for photocathodes.** CdS layers were deposited by the chemical bath deposition (CBD) method. Prior to CBD, the sample was pre-treated in a bath containing a solution of CdSO<sub>4</sub> (Sigma Aldrich, 99.99%) and NH<sub>4</sub>OH (Duksan, 28 wt%) at 60 °C for 10 min. CBD of CdS was performed by immersing the pre-treated sample in a solution containing CdSO<sub>4</sub>, thiourea (99%, Sigma Aldrich), deionised (DE) water, and NH<sub>4</sub>OH for 5 min at 60 °C. TiO<sub>2</sub> layers were deposited using an ALD system (Lucida D100, NCD Inc.). The ALD process was performed at 150 °C, with tetrakis(dimethylamido)titanium (TDMAT) and H<sub>2</sub>O as the Ti and O sources, respectively. A total of 600 ALD cycles were carried out, each of which comprised a TDMAT pulse of 0.3 s followed by 15 s of N<sub>2</sub> purging and a H<sub>2</sub>O pulse of 0.2 s followed by 15 s of N<sub>2</sub> purging. The approximate growth rate of TiO<sub>2</sub> was 0.55 Å per cycle, as estimated using an ellipsometer. The Pt catalyst was sputtered onto the TiO<sub>2</sub>-coated Sb<sub>2</sub>Se<sub>3</sub> electrode using an Auto Sputter Coater (Ted Pella, Redding, CA, USA) under an applied current of 10 mA for 120 s. A galvanostatic photo-deposition technique was used for RuO<sub>x</sub> deposition. The prepared photoelectrodes were immersed in a 1.3 mM solution of KRuO<sub>4</sub> at a current density of  $-28.3 \mu\text{A cm}^{-2}$  for 15 min under simulated 1 sun illumination.

**Preparation of BiVO<sub>4</sub> films.** All chemicals used in this study were of analytical grade and used without further purification. BiVO<sub>4</sub> film was prepared by a modified metal-organic decomposition method according to our previously reported procedure<sup>47</sup> with slight modifications. In brief, 291 mg of Bi(NO<sub>3</sub>)<sub>3</sub>·5H<sub>2</sub>O (99.8%; Kanto Chemicals) and 163 mg of VO(acac)<sub>3</sub> (98.0%; Sigma Aldrich) were dissolved in 15 mL of acetyl acetone (>99.0%; Kanto Chemicals). As the dopant solution, 0.03 M MoO<sub>2</sub>(acac)<sub>2</sub> (98.0%; Sigma Aldrich) in acetyl acetone (>99.0%; Kanto Chemicals) was prepared. A 0.2 M Bi(NO<sub>3</sub>)<sub>3</sub>·5H<sub>2</sub>O (99.8%; Kanto Chemicals) solution dissolved in acetic acid (>99.0%; Kanto Chemicals) was used to compensate the Mo precursor-added solution. For Mo doping, a Bi:(V+Mo) = 1:1 atomic ratio was used for preparing the 1% Mo:BiVO<sub>4</sub> films. To fabricate the BiVO<sub>4</sub> film, 35  $\mu\text{L}$  of the solution was dropped on a FTO glass sample (2 cm  $\times$  2.5 cm) and dried for 10 min in Ar atmosphere. The FTO glass (TEC 8; Pilkington) was cleaned using ethanol + 35 wt% H<sub>2</sub>O<sub>2</sub> (Samchun Chemical) used in a ratio of 5:1 under sonication ( $\sim 20$  min) and washed with copious amounts of ethanol and finally stored in 2-propanol before use. The greenish transparent precursor film was calcined at 550 °C for 30 min to form a yellow BiVO<sub>4</sub> film. After the annealing process, the 2 cm  $\times$  2.5 cm BiVO<sub>4</sub>/FTO was split to obtain photoanodes with a net



irradiation area of 0.36 cm<sup>2</sup> connected by silver paste and copper wire and sealed with epoxy resin.

**Hydrogen treatment of metal oxide films.** Hydrogen treatment was conducted using the borohydride decomposition method reported by Hao et al.<sup>48</sup>. First, 16 mmol of NaBH<sub>4</sub> (>98%; Sigma Aldrich) was introduced in a 200-mL alumina crucible and another smaller alumina bottle (15 mL) was introduced to the NaBH<sub>4</sub> powder. In this smaller bottle, an as-prepared metal oxide film (2 cm × 2.5 cm) was placed and finally the 200-mL alumina crucible was covered with an alumina cover. This reactor was placed in an already heated furnace at 500 °C for 30 min. Then the crucible was taken out from the furnace and cooled naturally.

**NiFeO<sub>x</sub> co-catalyst deposition on BiVO<sub>4</sub> film.** The NiFeO<sub>x</sub> co-catalysts were deposited by photo-assisted electrodeposition under air mass (AM) 1.5 G illumination according to a reported procedure<sup>49</sup>. In all, 60 mg of Fe(SO<sub>4</sub>)<sub>2</sub>·7 H<sub>2</sub>O (≥99%; Sigma Aldrich) and 20 mg of Ni(SO<sub>4</sub>)<sub>2</sub>·6H<sub>2</sub>O (99%; Sigma Aldrich) were put in a glass bottle and 200 mL of 0.5 M KHCO<sub>3</sub> (pH 8.3, purged with Ar gas for 30 min before use) was introduced, resulting in a transparent and yellow solution. For deposition, under illumination (AM 1.5 G, 100 mW cm<sup>-2</sup>), linear sweep voltammetry was conducted with a bias of -0.3 to 0.5 V against the reference electrode (Ag/AgCl) for 12–15 times with pre-treatment of -0.3 V for 5 s. Sequential linear sweep voltammetry resulted in reduced current density and over-deposition of NiFeO<sub>x</sub>. After deposition, the photoelectrode was taken out and washed with copious amounts of DI water. Right after being taken out, the photoelectrode showed a slightly darkened colour (Ni(OH)<sub>2</sub> species) but gradually changes to a colour identical to that of the photoelectrode before NiFeO<sub>x</sub> deposition. The photoelectrodes were stored in an Ar gas-filled bottle before use.

**Characterisation.** The surface morphology of Sb<sub>2</sub>Se<sub>3</sub> thin films were analysed via field-emission scanning electron microscope (JSM-7001F, JEOL Ltd, Tokyo, Japan). The crystallinity of the samples was investigated using XRD (MiniFlex 600, Rigaku, Tokyo, Japan) with Cu Kα radiation (λ = 1.54178 Å). The surface reflectance of the Sb<sub>2</sub>Se<sub>3</sub> thin films was measured using an ultraviolet-visible (UV-vis) spectrophotometer (V-670, JASCO, Easton, MD, USA). UV-Vis absorbance of BiVO<sub>4</sub> was recorded with a UV/Vis spectrometer (UV-2401PC, Shimadzu). As a reference, BaSO<sub>4</sub> powder was used. In addition, KPFM (SPA 400, Seiko Instrument Inc., Chiba, Japan) measurements were performed using a gold-coated cantilever (SI-DF3-A).

**Determination of PEC performance.** PEC measurements for Sb<sub>2</sub>Se<sub>3</sub> photocathodes were performed in a typical three-electrode system with an Ag/AgCl/KCl (4 M) reference electrode and a Pt wire counter electrode. The Sb<sub>2</sub>Se<sub>3</sub> photocathodes were submerged in an acidic (H<sub>2</sub>SO<sub>4</sub>, pH ~ 1) or a neutral (phosphate buffer, pH ~ 6.25) electrolyte and simulated solar light illumination. Calibration of the 1-sun level was performed using a standard Si reference cell certified by the Newport Corporation, consisting of a readout device and a 2 × 2 cm<sup>2</sup> calibrated solar cell made of monocrystalline silicon. During calibration, the Si reference cell was located at the same position of the sample for PEC measurement. The scan rate for the *J-V* curves was 5 mV s<sup>-1</sup>. For Sb<sub>2</sub>Se<sub>3</sub> photocathodes, the applied potentials were recorded against the RHE to allow comparison with previously reported results, employing the relationship  $E_{\text{RHE}} = E_{\text{Ag/AgCl}} + 0.059 \text{ pH} + 0.197$ . IPCE for Sb<sub>2</sub>Se<sub>3</sub> photocathodes was measured with an electrochemical workstation (Zennium, Zahner, Germany) combined with a potentiostat (PP211, Zahner, Germany) under monochromatic light.

PEC performance of the BiVO<sub>4</sub> photoanode was measured with a photoanode as the working electrode, Pt mesh as the counter electrode, and Ag/AgCl (3 M NaCl) as the reference electrode. The scan rate for the *J-V* curves was 20 mV s<sup>-1</sup>. For electrolyte, 0.5 M potassium phosphate (K<sub>2</sub>HPO<sub>4</sub> or KPi) buffer + 0.01 M V<sub>2</sub>O<sub>5</sub> (pH 7.0) was used as a standard electrolyte as reported previously for the borate buffer (pH 9.5). To accelerate dissolution of V<sub>2</sub>O<sub>5</sub>, it was placed in oven at 80 °C for 3 h. The pH of the KPi buffer barely changed (<0.01) while the pH of 8 or 9 showed a noticeable change that could be compensated by adding a small amount of 0.5 M KOH. Potentials were recorded with correction according to the Nernst relationship  $E_{\text{RHE}} = E_{\text{Ag/AgCl}} + 0.0591 \text{ pH} + 0.209$ , in which  $E_{\text{Ag/AgCl}}$  is the applied bias potential and 0.209 is a conversion factor from the Ag/AgCl electrode to the RHE scale. The electrochemical data for BiVO<sub>4</sub> photoanodes were recorded by using a potentiostat (IviumStat, Ivium Technologies). A 300 W Xenon lamp was used to produce simulated 1 sun light irradiation conditions (AM 1.5 G, 100 mW cm<sup>-2</sup>) employing a solar simulator (Oriol 91160) with an AM 1.5 G filter calibrated with a reference cell certified by the National Renewable Energy Laboratories, USA.

For the BiVO<sub>4</sub>-Sb<sub>2</sub>Se<sub>3</sub> tandem cell, black masked (0.32–0.36 cm<sup>2</sup>) photoelectrodes were aligned with a spacing of ~0.5 cm in a single electrolyte bed reactor. Photocurrent of Sb<sub>2</sub>Se<sub>3</sub> was recorded with or without the BiVO<sub>4</sub> photoelectrode (fully modified, NiFeO<sub>x</sub>/H<sub>2</sub>Mo:BiVO<sub>4</sub>) under backward scan (-0.5–0 V<sub>RHE</sub>). The BiVO<sub>4</sub> photoelectrode was scanned in the forward scan (0.2–1.4 V<sub>RHE</sub>). For the BiVO<sub>4</sub>-Sb<sub>2</sub>Se<sub>3</sub> two-electrode full cell, BiVO<sub>4</sub> was set as the working electrode and Sb<sub>2</sub>Se<sub>3</sub> was set as the counter electrode. Bias was applied towards the counter electrode and thus 0 V against the counter electrode indicated a 0 V potential applied to the full cell. For linear sweep, forward scan was applied for

the BiVO<sub>4</sub>-Pt rod (0.3–1.3 V) or BiVO<sub>4</sub>-Sb<sub>2</sub>Se<sub>3</sub> (-0.3 to 0.5 V). All scans were performed with 10 s of pre-treatment at the initial potential at a speed of 20 mV s<sup>-1</sup>.

IPCE measurements for BiVO<sub>4</sub> and Sb<sub>2</sub>Se<sub>3</sub> behind BiVO<sub>4</sub> were conducted using a 300 W Xe lamp as the light source with a liquid infrared filter and a monochromator (Oriol Cornerstone 130 1/8 m monochromator) with a bandwidth limit of 5 nm. The intensity of light was measured before IPCE measurements by a photodiode detector (Oriol 70260). Calculation of IPCE was carried out according to the equation:

$$\text{IPCE}(\%) = \frac{1240 \times J}{\lambda \times P} \times 100 \quad (1)$$

where *J* = photocurrent density (mA cm<sup>-2</sup>), *P* = light power density (mW cm<sup>-2</sup>) at λ, and λ = wavelength of incident light (nm). *J* was gathered under the condition that the PEC cell individually installed and the constant potential applied for a photoelectrode and wavelength of illuminated beam (1 cm × 1 cm) was periodically changed. The active area of the characterised photoelectrode was preferably smaller than this beam source (0.32–0.36 cm<sup>2</sup>). The scanning wavelength range was 300–1100 nm with an interval of 10 nm/7 s.

## Data availability

The data that support the plots within this paper and other findings of this study are available from the corresponding author upon reasonable request. The source data underlying Figs. 2, 3e, f, 4b–d, 5b–e, and 6 and Supplementary Figs. 2, 3, 4, 5c, 7, 8, 9, 10, 11a, 13, 14, 15, 16, 17, 18b–d, 19, and 21a are provided as a Source Data file.

Received: 2 August 2019; Accepted: 24 January 2020;

Published online: 13 February 2020

## References

- Cheng, W.-H. et al. Monolithic photoelectrochemical device for direct water splitting with 19% efficiency. *ACS Energy Lett.* **3**, 1795–1800 (2018).
- Turner, J. A. Shining a light on solar water splitting—response. *Science* **344**, 469–470 (2014).
- Sivula, K. & Van De Krol, R. Semiconducting materials for photoelectrochemical energy conversion. *Nat. Rev. Mater.* **1**, 15010 (2016).
- Kim, J. H., Hansora, D., Sharma, P., Jang, J.-W. & Lee, J. S. Toward practical solar hydrogen production—an artificial photosynthetic leaf-to-farm challenge. *Chem. Soc. Rev.* **48**, 1908–1971 (2019).
- Yao, T., An, X., Han, H., Chen, J. Q. & Li, C. Photoelectrocatalytic materials for solar water splitting. *Adv. Energy Mater.* **8**, 1800210 (2018).
- Hu, S., Xiang, C., Haussener, S., Berger, A. D. & Lewis, N. S. An analysis of the optimal band gaps of light absorbers in integrated tandem photoelectrochemical water-splitting systems. *Energy Environ. Sci.* **6**, 2984–2993 (2013).
- Pinaud, B. A. et al. Technical and economic feasibility of centralized facilities for solar hydrogen production via photocatalysis and photoelectrochemistry. *Energy Environ. Sci.* **6**, 1983–2002 (2013).
- Fujishima, A. & Honda, K. Electrochemical photolysis of water at a semiconductor electrode. *Nature* **238**, 37–38 (1972).
- Tamirat, A. G., Rick, J., Dubale, A. A., Su, W.-N. & Hwang, B.-J. Using hematite for photoelectrochemical water splitting: a review of current progress and challenges. *Nanoscale Horiz.* **1**, 243–267 (2016).
- Kim, J. H. & Lee, J. S. Elaborately modified BiVO<sub>4</sub> photoanodes for solar water splitting. *Adv. Mater.* **31**, 1806938 (2019).
- Paracchino, A., Laporte, V., Sivula, K., Grätzel, M. & Thimsen, E. Highly active oxide photocathode for photoelectrochemical water reduction. *Nat. Mater.* **10**, 456 (2011).
- Yang, W. et al. Molecular chemistry-controlled hybrid ink-derived efficient Cu<sub>2</sub>ZnSnS<sub>4</sub> photocathodes for photoelectrochemical water splitting. *ACS Energy Lett.* **1**, 1127–1136 (2016).
- Yu, Y.-X. et al. Solution-processed Cu<sub>2</sub>S photocathodes for photoelectrochemical water splitting. *ACS Energy Lett.* **3**, 760–766 (2018).
- Oh, Y., Yang, W., Kim, J., Jeong, S. & Moon, J. Enhanced photocurrent of transparent CuFeO<sub>2</sub> photocathodes by self-light-harvesting architecture. *ACS Appl. Mater. Interfaces* **9**, 14078–14087 (2017).
- Song, A. et al. Cu:NiO as a hole-selective back contact to improve the photoelectrochemical performance of CuBi<sub>2</sub>O<sub>4</sub> thin film photocathodes. *J. Mater. Chem. A* **7**, 9183–9194 (2019).
- Zhang, L. et al. Solution-processed CuSb<sub>2</sub>S<sub>4</sub> thin film: a promising earth-abundant photocathode for efficient visible-light-driven hydrogen evolution. *Nano Energy* **28**, 135–142 (2016).
- Huang, X. et al. Simple eco-friendly synthesis of the surfactant free SnS nanocrystal toward the photoelectrochemical cell application. *Sci. Rep.* **7**, 16531 (2017).
- Yang, W. & Moon, J. Rapid advances in antimony triselenide photocathodes for solar hydrogen generation. *J. Mater. Chem. A* **7**, 20467 (2019).

19. Wang, L. et al. Stable 6%-efficient  $\text{Sb}_2\text{Se}_3$  solar cells with a ZnO buffer layer. *Nat. Energy* **2**, 17046 (2017).
20. Chen, C. et al. Characterization of basic physical properties of  $\text{Sb}_2\text{Se}_3$  and its relevance for photovoltaics. *Front. Optoelectron.* **10**, 18–30 (2017).
21. Ghosh, G. The Sb–Se (antimony–selenium) system. *J. Phase Equilibria* **14**, 753–763 (1993).
22. Prabhakar, R. R. et al. Photocorrosion-resistant  $\text{Sb}_2\text{Se}_3$  photocathodes with earth abundant MoSx hydrogen evolution catalyst. *J. Mater. Chem. A* **5**, 23139–23145 (2017).
23. Kim, J. et al. Self-oriented  $\text{Sb}_2\text{Se}_3$  nanoneedle photocathodes for water splitting obtained by a simple spin-coating method. *J. Mater. Chem. A* **5**, 2180–2187 (2017).
24. Yang, W. et al. Adjusting the anisotropy of 1D  $\text{Sb}_2\text{Se}_3$  nanostructures for highly efficient photoelectrochemical water splitting. *Adv. Energy Mater.* **8**, 1702888 (2018).
25. Tan, J. et al. Fullerene as a photoelectron transfer promoter enabling stable  $\text{TiO}_2$ -protected  $\text{Sb}_2\text{Se}_3$  photocathodes for photo-electrochemical water splitting. *Adv. Energy Mater.* **9**, 1900179 (2019).
26. Lee, H. et al. Cu-doped NiOx as effective hole-selective layer for high-performance  $\text{Sb}_2\text{Se}_3$  photocathode for photoelectrochemical water splitting. *ACS Energy Lett.* **4**, 995–1003 (2019).
27. Park, J. et al. Efficient solar to hydrogen conversion from neutral electrolytes using morphology-controlled  $\text{Sb}_2\text{Se}_3$  light absorber. *ACS Energy Lett.* **4**, 517–526 (2019).
28. Phillips, L. J. et al. Current enhancement via a  $\text{TiO}_2$  window layer for CSS  $\text{Sb}_2\text{Se}_3$  solar cells: performance limits and high Voc. *IEEE J. Photovolt.* **9**, 544–551 (2019).
29. Major, J. D. et al. A low-cost non-toxic post-growth activation step for CdTe solar cells. *Nature* **511**, 334–337 (2014).
30. Guo, Q. et al. The growth of a  $\text{CH}_3\text{NH}_3\text{PbI}_3$  thin film using simplified close space sublimation for efficient and large dimensional perovskite solar cells. *Energy Environ. Sci.* **9**, 1486–1494 (2016).
31. Hutter, O. S., Phillips, L. J., Durose, K. & Major, J. D. 6.6% efficient antimony selenide solar cells using grain structure control and an organic contact layer. *Sol. Energy Mater. Sol. Cells* **188**, 177–181 (2018).
32. Yang, W. et al. Time-resolved observations of photo-generated charge-carrier dynamics in  $\text{Sb}_2\text{Se}_3$  photocathodes for photoelectrochemical water splitting. *ACS Nano* **12**, 11088–11097 (2018).
33. Zhang, J. et al. Alternative back contacts for  $\text{Sb}_2\text{Se}_3$  solar cells. *Sol. Energy* **182**, 96–101 (2019).
34. Tilley, S. D., Schreier, M., Azevedo, J., Stefik, M. & Graetzel, M. Ruthenium oxide hydrogen evolution catalysis on composite cuprous oxide water-splitting photocathodes. *Adv. Funct. Mater.* **24**, 303–311 (2014).
35. Chen, C. et al. Efficiency improvement of  $\text{Sb}_2\text{Se}_3$  solar cells via grain boundary inversion. *ACS Energy Lett.* **3**, 2335–2341 (2018).
36. Vishwakarma, M. et al. A direct measurement of higher photovoltage at grain boundaries in CdS/CZTSe solar cells using KPFM technique. *Sol. Energy Mater. Sol. Cells* **183**, 43–40 (2018).
37. Kim, G. Y. et al. Nanoscale investigation of surface potential distribution of  $\text{Cu}_2\text{ZnSn}(\text{S},\text{Se})_4$  thin films grown with additional NaF layers. *Nano Convergence* **1**, 27 (2014).
38. Luo, J. et al.  $\text{Cu}_2\text{O}$  nanowire photocathodes for efficient and durable solar water splitting. *Nano Lett.* **16**, 1848–1857 (2016).
39. Prévot, M. S. & Sivula, K. Photoelectrochemical tandem cells for solar water splitting. *J. Phys. Chem. C* **117**, 17879–17893 (2013).
40. Mayer, M. T. Photovoltage at semiconductor–electrolyte junctions. *Curr. Opin. Electrochem.* **2**, 104–110 (2017).
41. Vijeelaar, W. et al. Spatial decoupling of light absorption and catalytic activity of Ni–Mo-loaded high-aspect-ratio silicon microwire photocathodes. *Nat. Energy* **3**, 185 (2018).
42. Kaneko, H., Minegishi, T., Kobayashi, H., Kuang, Y. & Domen, K. Suppression of poisoning of photocathode catalysts in photoelectrochemical cells for highly stable sunlight-driven overall water splitting. *J. Chem. Phys.* **150**, 041713 (2019).
43. Kobayashi, H. et al. Development of highly efficient  $\text{CuIn}_{0.5}\text{Ga}_{0.5}\text{Se}_2$ -based photocathode and application to overall solar driven water splitting. *Energy Environ. Sci.* **11**, 3003–3009 (2018).
44. Pan, L. et al. Boosting the performance of  $\text{Cu}_2\text{O}$  photocathodes for unassisted solar water splitting devices. *Nat. Catalysis* **1**, 412 (2018).
45. Higashi, T. et al. Overall water splitting by photoelectrochemical cells consisting of  $(\text{ZnSe})_{0.85}(\text{CuIn}_{0.7}\text{Ga}_{0.3}\text{Se}_2)_{0.15}$  photocathodes and  $\text{BiVO}_4$  photoanodes. *Chem. Commun.* **53**, 11674–11677 (2017).
46. Wick-Jaliat, R. et al. Stable and tunable phosphonic acid dipole layer for band edge engineering of photoelectrochemical and photovoltaic heterojunction devices. *Energy Environ. Sci.* **12**, 1901–1909 (2019).
47. Kim, J. H. et al. Wireless solar water splitting device with robust cobalt-catalyzed, dual-doped  $\text{BiVO}_4$  photoanode and perovskite solar cell in tandem: a dual absorber artificial leaf. *ACS Nano* **9**, 11820–11829 (2015).
48. Hao, Y., Deng, J., Zhou, L., Sun, X. & Zhong, J. Depth-reduction induced low onset potential of hematite photoanodes for solar water oxidation. *RSC Adv.* **5**, 31086–31090 (2015).
49. Li, F. et al. An iron-based thin film as a highly efficient catalyst for electrochemical water oxidation in a carbonate electrolyte. *Chem. Commun.* **52**, 5753–5756 (2016).

## Acknowledgements

This work was supported by a National Research Foundation (NRF) of Korea grant (No. 2012R1A3A2026417); a Creative Materials Discovery Program (NRF-2018M3D1A1058793) funded by the Ministry of Science and ICT; the Korea Center for Artificial Photosynthesis (KCAP, No. 2009–0093880), funded by the MSIT; Project No. 10050509 funded by the MOTIE of Republic of Korea; and the UK EPSRC project number EP/N014057/1.

## Author contributions

W.Y. conceived the idea, organised the collaboration, conducted experiments, analysed the data, and wrote the manuscript. J.H.K. prepared the  $\text{BiVO}_4$  photoanodes, tested the tandem device, and co-wrote the manuscript. O.S.H. and L.J.P. prepared and optimised the  $\text{Sb}_2\text{Se}_3$  thin films via the CSS method. J.T., J.P. and H.L. assisted in device optimisation and data analysis for the  $\text{Sb}_2\text{Se}_3$  photocathodes. J.D.M. helped to the idea and manuscript preparation. J.S.L. directed the research and contributed to the writing of the manuscript. J.M. designed and supervised the project, directed the research, and contributed to the writing of the manuscript.

## Competing interests

The authors declare no competing interests.

## Additional information

Supplementary information is available for this paper at <https://doi.org/10.1038/s41467-020-14704-3>.

Correspondence and requests for materials should be addressed to J.D.M., J.S.L. or J.M.

Peer review information *Nature Communications* thanks the anonymous reviewers for their contributions to the peer review of this work. Peer review reports are available.

Reprints and permission information is available at <http://www.nature.com/reprints>

Publisher's note Springer Nature remains neutral with regard to jurisdictional claims in published maps and institutional affiliations.



**Open Access** This article is licensed under a Creative Commons Attribution 4.0 International License, which permits use, sharing, adaptation, distribution and reproduction in any medium or format, as long as you give appropriate credit to the original author(s) and the source, provide a link to the Creative Commons license, and indicate if changes were made. The images or other third party material in this article are included in the article's Creative Commons license, unless indicated otherwise in a credit line to the material. If material is not included in the article's Creative Commons license and your intended use is not permitted by statutory regulation or exceeds the permitted use, you will need to obtain permission directly from the copyright holder. To view a copy of this license, visit <http://creativecommons.org/licenses/by/4.0/>.

© The Author(s) 2020